Intrinsically narrowband pair photon generation in microstructured fibres

Olivier Alibart, Alex Clark, Bryn Bell, Jérémie Fulconis, Matthäus M Halder, Ben Cemlyn, Chunle Xiong, William J Wadsworth, John G Rarity

Intrinsically narrowband pair photon generation in microstructured fibres

Alex Clark[1,4]**, Bryn Bell**[1]**, Jérémie Fulconis**[1]**,
Matthäus M Halder**[1]**, Ben Cemlyn**[1]**, Olivier Alibart**[2]**,
Chunle Xiong**[3]**, William J Wadsworth**[3] **and John G Rarity**[1]

[1] Centre for Communications Research, Department of Electrical and Electronic Engineering, University of Bristol, Merchant Venturers Building, Woodland Road, Bristol BS8 1UB, UK
[2] Laboratoire de Physique de la Matière Condensée, Unité Mixte de Recherche 6622, Centre National de la Recherche Scientifique, Université de Nice-Sophia Antipolis, Parc Valrose 06108, Nice 2, France
[3] Centre for Photonics and Photonic Materials, Department of Physics, University of Bath, Claverton Down, Bath BA2 7AY, UK
E-mail: alex.clark@bristol.ac.uk

Abstract. In this paper, we study the tailoring of photon spectral properties generated by four-wave mixing in a birefringent photonic crystal fibre (PCF). The aim is to produce intrinsically narrow-band photons and hence to achieve high non-classical interference visibility and generate high-fidelity entanglement without any requirement for spectral filtering, leading to high effective detection efficiencies. We show unfiltered Hong–Ou–Mandel interference visibilities of 77% between photons from the same PCF and 80% between separate sources. We compare results from modelling the PCF to these experiments and analyse photon purities.

[4] Author to whom any correspondence should be addressed.

Contents

1. Introduction

Single photons are at the heart of optical quantum technologies, such as quantum cryptography [1], quantum computing [2] and quantum metrology [3]. These applications mainly rely on non-classical interference and so one constraining factor is that the photons must be in a pure quantum state [4]. One way to generate single photons is to use pair photon sources based on parametric down-conversion or four-wave mixing (FWM), where the detection of one photon of the pair can herald the presence of the second photon [5]. However, owing to energy and momentum correlations, the heralded photon usually ends up in a mixed state [6]. The common way to counteract this issue is then to strongly filter the photon pair at the cost of losses, which significantly reduces the overall efficiency μ of detecting a photon. In a multi-photon experiment involving n photons (such as a cascaded controlled-NOT (CNOT) gate), the overall probability of detection scales as μ^n, meaning that a high effective detection efficiency is essential. It has recently been suggested that naturally narrow band phase matching can be achieved in the case of a birefringent photonic crystal fibre (PCF) when photon pairs are created in a polarization orthogonal to that of the pump light [7]. In this paper, we study the tailoring of photon spectral properties generated by FWM in such a birefringent PCF. The aim is to produce intrinsically narrow-band photons and hence to achieve high non-classical interference visibility without any requirement for spectral filtering. We examine experimentally how the phase-matching of several different PCFs compares with theoretical expectations, and perform non-classical interference to measure the purity—first between photons from two separate PCFs, and then from a single PCF pumped in two directions using a Sagnac loop configuration. We then use simulations to look at how the purity of the photons' state depends on the fibre parameters and the pump laser, and compare these with the experimental results. Finally, we use the Sagnac setup to demonstrate a PCF source of polarization-entangled photon pairs, and perform quantum state tomography (QST) on the generated photons so as to quantify the entanglement present.
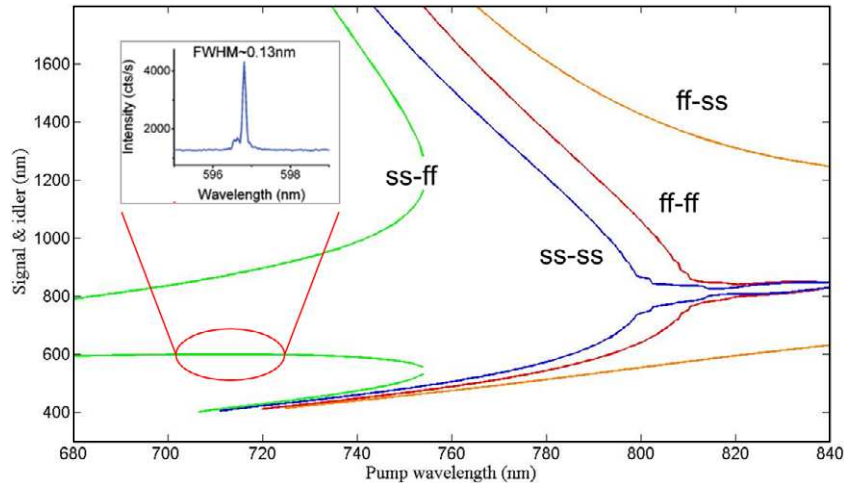
Figure 1. Signal and idler wavelengths as a function of the pump in a birefringent fibre.

2. Four-wave mixing (FWM) in birefringent fibres

At the quantum level, the FWM process can be regarded to be the virtual absorption of two pump (p) photons and the subsequent creation of a signal (s) and idler (i) photon pair. The output state of the pair is then represented by

$$|\Psi\rangle = \int \int d\omega_s \, d\omega_i F(\omega_s, \omega_i) |\omega_s\rangle |\omega_i\rangle, \tag{1}$$

where the joint spectral amplitude (JSA) $F(\omega_s, \omega_i)$ is equal to the product of the pump amplitude $\alpha(\omega_s + \omega_i)$ and a phase-matching function $\phi(\omega_s, \omega_i)$.

The process then has to satisfy the energy conservation,

$$\Delta\omega = 2\omega_p - \omega_s - \omega_i = 0, \tag{2}$$

and a significant buildup of amplitude in a length of fibre requires phase matching,

$$\Delta k = 2\frac{n_p \omega_p}{c} - \frac{n_s \omega_s}{c} - \frac{n_i \omega_i}{c} - 2\gamma P_p = 0, \tag{3}$$

where $n_{p,s,i}$ are the refractive indices of the medium at pump, signal and idler wavelengths, P_p is the peak pump power, and γ is the nonlinear coefficient of the fibre,

$$\gamma = 2\pi n_2 / \lambda_p A_{eff}, \tag{4}$$

with $n_2 = 2 \times 10^{-20} \, \text{m}^2 \, \text{W}^{-1}$ being the nonlinear refractive index of silica and A_{eff} the effective cross-sectional area of the fibre mode [8].

For a birefringent fibre, the refractive index will be different along the slow (s) and fast (f) axes. Solving equations (2) and (3) will result in four different solutions, as illustrated in figure 1. The pair is created either along the same axis as the pump photons ($ss \rightarrow ss$ and $ff \rightarrow ff$) or along the axis orthogonal to that of the pump ($ss \rightarrow ff$ and $ff \rightarrow ss$). In the fabrication process of the fibre, a careful choice of n_p and n_i can lead to a situation where, at an appropriate λ_p, the group velocity of the pump is equal to that of the idler [6]. This situation corresponds to the zero-slope region of the $ss \rightarrow ff$ curve in figure 1, giving rise to signal photons that are intrinsically narrow band and insensitive to pump wavelength over a short range. In this
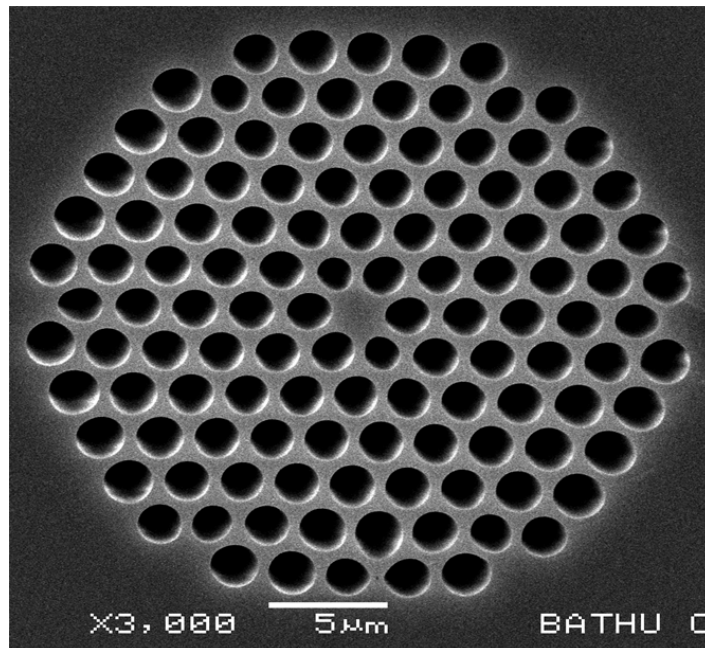
Figure 2. Scanning electron microscope (SEM) image of the central region of PCF A. The birefringence required was introduced by reducing the size of two holes adjacent to the core (at 11 o'clock and 5 o'clock).

case, the photon pairs are created in an uncorrelated spectral state with a JSA that is factorable; $F(\omega_s, \omega_i) = S(\omega_s).I(\omega_i)$, and the detection of one photon of the pair can then be used to herald the other in a pure quantum state.

3. Experimental study

In order to investigate the generation of photons in an intrinsically pure state, we have fabricated a set of birefringent PCFs (-A, -B and -C) designed to have a zero dispersion wavelength (ZDW) of around 780–800 nm. These fibres have similar dispersion profiles but exhibit slightly different birefringence due to different air hole sizes in the cladding. To introduce birefringence, the diameter of the holes at 11 o'clock and 5 o'clock is slightly reduced when compared with other holes surround the core, as can be seen in figure 2. These PCFs have inflated air holes; hence holes near the core are not circular and it is not possible to define a uniform hole diameter and pitch. By determining the hole shapes using SEM images of the fibres, we calculate the air-filling fraction in the cladding as 50, 72 and 82% with average core diameters of 2.36, 2.55 and 2.44 μm, and the diameter of modified holes near the core was reduced by 4, 2 and 1%, respectively, for PCF-A, -B and -C. The ZDW and the birefringence were chosen to satisfy the cross-polarization phase matching $ss \rightarrow ff$ in the pumping region 700–740 nm accessible by our Ti : sapphire laser. The zero-slope section of the signal phase matching previously shown in figure 1 was made to sit in the region 600–650 nm. In this manner, matching idler photons are emitted in a range where Si APDs are still efficient (800–870 nm) but are far enough from the pump wavelength to keep the Raman background low.

We used a plane-wave method [9] to calculate the dispersion curves and retrieve phase-matching solutions for the three fabricated PCFs. In these calculations, the shapes and positions
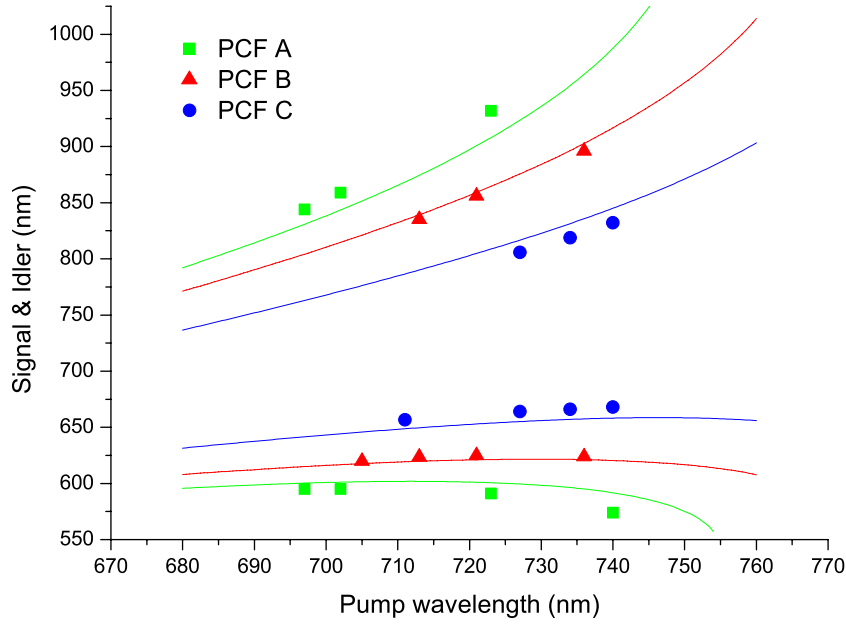
Figure 3. Theoretical phase-matching curves and the corresponding experimental results in the $ss \rightarrow ff$ cross-polarization phase-matching case, for a set of three birefringent PCFs (-A, -B and -C).

of the air holes were taken from SEM images. We show in figure 3 the theoretical phase matching for the $ss \rightarrow ff$ cross-polarization case and the corresponding experimental results when pumping from 700 to 740 nm, which are in good agreement.

3.1. Spectral bandwidths

We now focus on the zero-slope region of the phase matching, and study the spectral bandwidth of signal photons as a function of fibre length. As described in [10], the bandwidth equation of generated photons is given by

$$\Delta\omega_s = \frac{2\pi c}{|\mathcal{N}_s - \mathcal{N}_i|\, L} + 2\left|\frac{\mathcal{N}_i - \mathcal{N}_p}{\mathcal{N}_s - \mathcal{N}_i}\right|\Delta\omega_p, \tag{5}$$

where L is the fibre length, $\mathcal{N}_l = [\omega_l \frac{\partial n_l}{\partial\omega}|_{\omega_l} + n_l]$ ($l = $ i, s, p) is the fibre group index at ω_l and $\Delta\omega_p$ is the pump bandwidth.

This equation is thus driven by two terms, one corresponding to the natural bandwidth of the phase matching, and a second related to the pump bandwidth broadening. The first is proportional to the inverse of the fibre length, whereas the second is proportional to the difference between the idler and pump group index (and the slope of the phase-matching curve). In our case, $n_i - n_p = 0$, which means that the signal bandwidth is insensitive to pump bandwidth and thus only behaves as the inverse of the fibre length. This is verified by our measurement shown in figure 4, where we can see the experimental data and the corresponding $1/L$ fitting curve. This study was limited by the fact that homogeneity over the length of fibre is very difficult to control during the fabrication process and 1 m of fibre is the longest usable length. As we shall see in the next section, this limitation will also restrain our experimental study on purity.
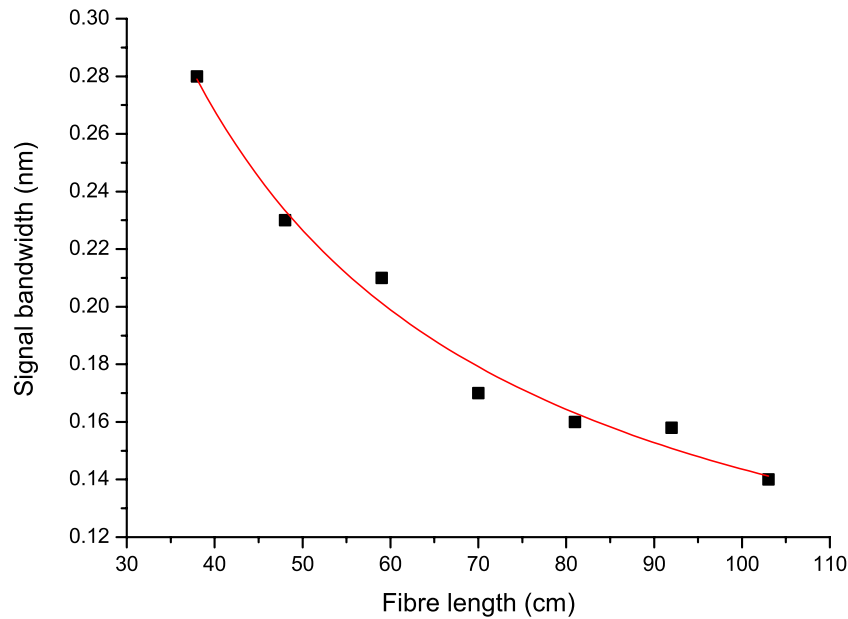
Figure 4. Spectral bandwidth of the signal photons as a function of fibre length and a $1/L$ fitting curve.
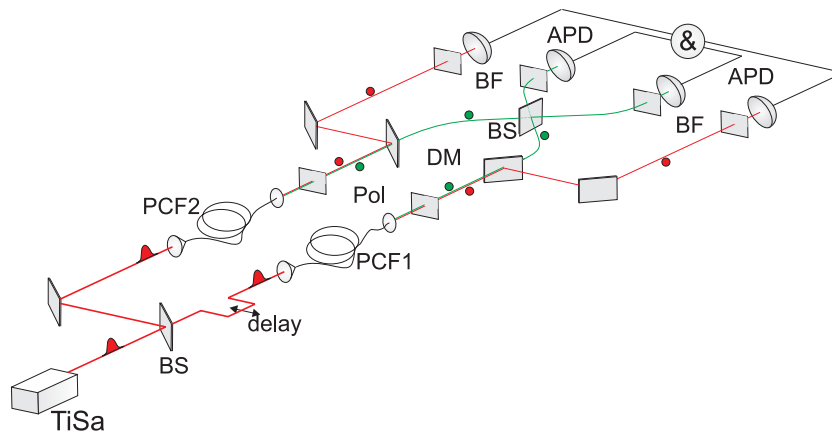
Figure 5. Schematic representation of the experimental setup to demonstrate quantum interference between photons generated in separate fibres. A full description is given in the text.

3.2. Quantum interference

In order to experimentally test the purity of our heralded single photons, we performed a Hong–Ou–Mandel (HOM) experiment [11] using heralded single photons generated from independent PCF sources. Figure 5 shows the setup of the experiment. Among the three PCFs fabricated, we decided to use PCF-A, which has the highest birefringence. In this manner, pumping at 705 nm corresponding to the zero-slope region of the signal curve, phase matching is satisfied for generation of signal and idler photons at 597 and 860 nm, respectively. At these wavelengths, the detection efficiency is high (∼60% for the signal and ∼40% for the idler) and the Raman background in the idler arm remains low. We use a mode-locked Ti : sapphire pump

Figure 6. HOM interference visibility plotted as a function of pump bandwidth.

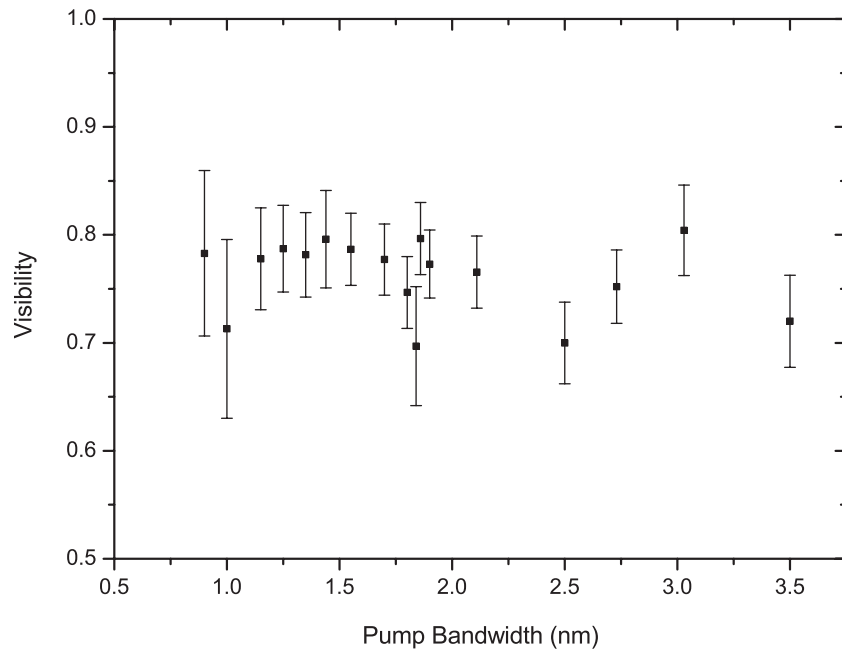laser emitting 100 fs pulses at 705 nm with a repetition rate of 80 MHz, which passes through a tuneable filter allowing control of the bandwidth from 7 nm ($\sim$100 fs) to 0.25 nm ($\sim$3 ps). Within this full range, the signal bandwidth remains constant at $\sim$0.15 nm, demonstrating its independence of pump wavelength in this region. The laser has an output power of 800 mW, which is filtered to 40 mW and remains reasonably stable over the duration of the experiment. Any small fluctuations in power will have a negligible effect on the output photon spectra, as the phase matching is dominated by the birefringence introduced and not by the γP term. The light is then sent onto a 50 : 50 beam splitter (BS) to pump two separate 40 cm-long pieces of PCF-A. At the output of each PCF, a polarizer (Pol) oriented with the polarization of the pairs is used to filter the remaining pump light in the orthogonal polarization, and a dichroic mirror (DM) centred at 700 nm is used to split signal and idler photons into two different arms. In order to get rid of the residual pump light, two bandpass filters (BFs) of 40 and 10 nm bandwidths are used in the signal and idler arms, respectively. The idler photons of each source are then launched into single-mode fibres, and the signal photons into a single-mode 50:50 coupler with polarization controllers (PCs) in one of the input arms. Since the photons are well-mode-matched to these optical fibres and they have not undergone narrow spectral filtering, we are able to achieve high overall lumped efficiencies for both sources of $\eta_s = 0.25$ and $\eta_i = 0.18$ of signal and idler, respectively. All four outputs are finally connected to silicon avalanche photodiodes (APD) linked to a fourfold coincidence measurement apparatus (&).

A retro-reflector mounted on a micrometric translation stage in one arm of the interferometer allows us to vary the temporal overlap (δt) between the two photon pairs. When the two signal photons are made to arrive simultaneously at the BS ($\delta t = 0$), we can see a reduction in the fourfold coincidence count rate, which is a measure of the purity of our heralded state. Using the tuneable filter, we performed this experiment at different pump bandwidths. The visibility of the HOM dip as a function of pump bandwidth is plotted in figure 6. The visibility
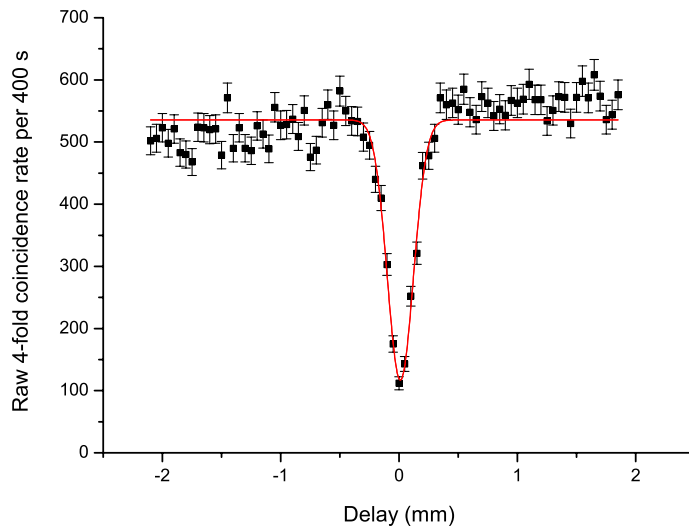
Figure 7. Coincidences as a function of delay position with a pump bandwidth of 3.03 nm.

seems reasonably constant across the range shown; with a weak peak when the pump bandwidth is ∼3.03 nm and where a $80 \pm 2.5\%$ visibility dip can be observed (see figure 7). Although a clearly non-classical result, the visibility falls below the theoretical maximum of 100%. A possible reason for this is that the separate fibres produce signal photons with slightly different spectra due to variation in the fabrication process. In order to investigate this, we performed a further experiment.

3.3. Quantum interference from a bi-directional source

To test whether this limit in the visibility of the two-photon interference was due to the use of two separate lengths of PCF, we decided to try a method of generating two pairs of photons in one length of fibre, as was previously carried out in [12], to ensure that the photons are spectrally indistinguishable. In this scheme, the filtered pump pulse from the Ti : sapphire laser is separated into two and set to counter-propagate through opposite inputs of the same fibre, but on the same principle axis. This is achieved through a Sagnac loop configuration, which is also useful in generating entangled photons.

The setup of this experiment can be seen in figure 8. A 20 cm length of the birefringent PCF used previously is set up on two alignment stages with the ends able to rotate about the axis of propagation, allowing the fibre to be aligned along either birefringent axis. A polarizing beam splitter (PBS) is then placed at the point where the output modes of both ends of the PCF meet. It can be seen at this point that if the pump pulse is sent through the PBS, it can travel to either input of the PCF dependent on its polarization. The PCF input for pumping clockwise around the loop is rotated such that the slow axis is horizontal, whereas the input for pumping counter-clockwise has the slow-axis orientated vertically.

Pump photons propagating in a counter-clockwise direction are horizontally polarized and therefore these photons generate vertically polarized signal and idler photons due to the cross-polar phase-matching scheme. As the fibre is twisted through 90°, the signal and idler polarizations are rotated so as to be horizontally polarized; they exit through the PBS towards
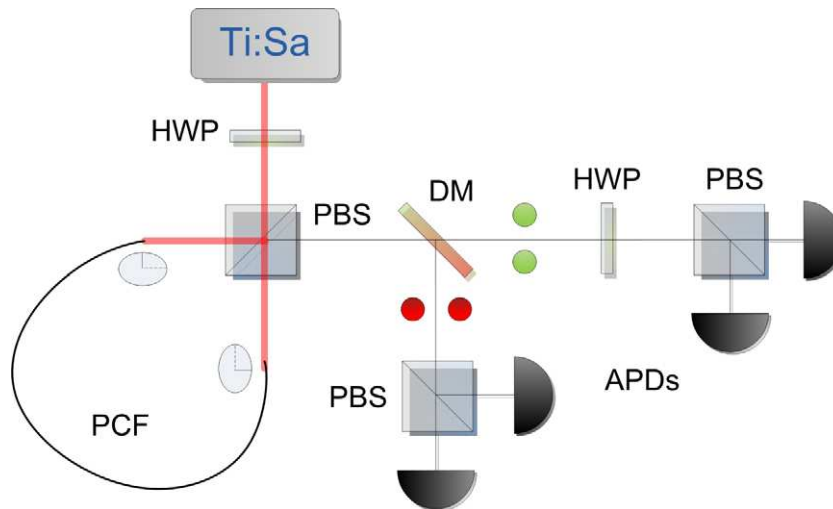
Figure 8. The setup used to generate two pairs of photons from one PCF and perform a polarization-based HOM dip between a photon of each pair. Pulses from a Ti : sapphire laser are filtered and set to diagonal polarization so that the beam can counter-propagate round a loop of PCF, which is twisted so that the birefringent axis is aligned with the PBS output polarization. Pairs of photons with orthogonal polarizations are generated in each direction and then split at a DM. Detecting the horizontal and vertical idler photons heralds the signal photons, which are made to interfere on a further PBS using a half wave plate (HWP) before detection.

the detectors, leaving the output state as $|\psi\rangle_{\text{out}} = |H\rangle_s|H\rangle_i$. If the pump photons propagate in the clockwise direction, then the same processes will occur but $H \to V$ and $V \to H$. The vertically polarized pump photons $|\psi\rangle_{\text{in}} = |V\rangle_{P_1}|V\rangle_{P_2}$ generate horizontally polarized signal and idler photons $|\psi\rangle = |H\rangle_s|H\rangle_i$ that are then transformed back to vertical polarization by the twist in the fibre, such that $|\psi\rangle_{\text{out}} = |V\rangle_s|V\rangle_i$. These photons therefore exit again through the same output of the PBS as in the counter-clockwise case. Any pump photons that do not generate signal and idler photons are rejected back towards the pump laser.

If the input power is large enough, there is a finite probability of generating a pair of photons in both directions; hence we have the state

$$|\psi\rangle_{\text{out}} = |H\rangle_s|H\rangle_i|V\rangle_s|V\rangle_i \qquad (6)$$

all in the same single spatial mode. By inserting a DM, we can split the signal and idler photons into separate modes for heralding and analysis. All of the photons are collected into single-mode fibres with PCs to correct for any rotation caused by bends in the fibre and are sent to analysis benches. Idler photons are split into two polarization modes by a PBS and are then detected using silicon APDs as before, heralding signal photons in the setup. Signal photons are passed through a HWP in a rotation mount and are then sent through another PBS; this is followed by detection. Here, we use the HWP in the signal arm to perform a polarization analogue of the standard delay-based HOM dip, where the polarizations of the signal photons are rotated from H and V to $+45°$ and $-45°$, respectively, and the degree of suppression of the heralded (and therefore fourfold) coincidence detection rate across all output ports characterizes the purity and distinguishability of the incident photons [12]. With a pump bandwidth of ~ 0.7 nm and signal
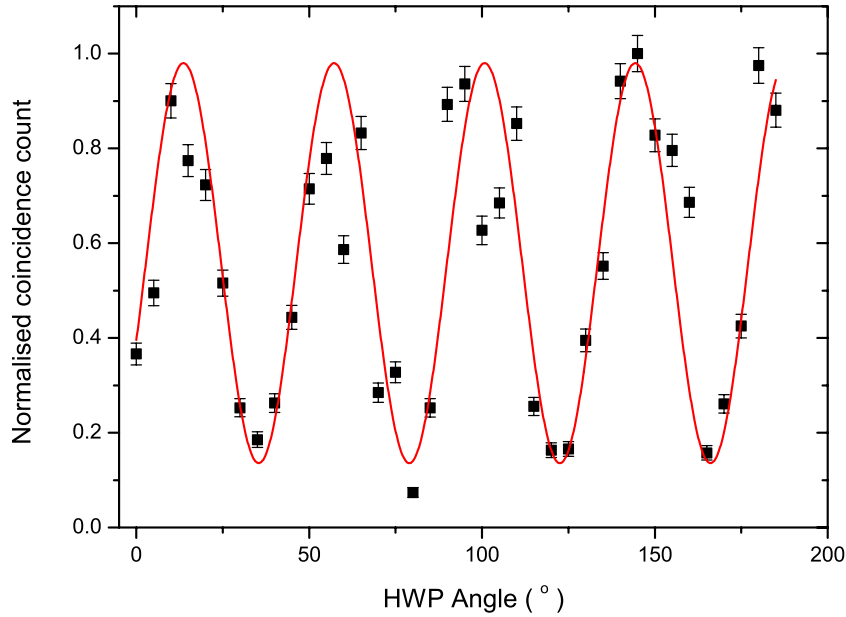
Figure 9. Interference fringes in the coincidences detected as the polarization is varied with a HWP.

and idler filtering that is the same as for the previous HOM dip experiment, we see in figure 9 fringes of $\sim 77\%$ visibility, again below the theoretical maximum of $\sim 100\%$.

4. Schmidt number optimization

To discern whether there is an inherent purity limitation with the PCF used, we construct a model to compare with the experiment. The purity of the heralded state is determined by the degree of factorability of the JSA [13] and it varies with pump wavelength, fibre length, pump bandwidth and fibre geometry (by which the group velocity of the signal, idler and pump wavelengths can be controlled). We have developed a piece of software to optimize these variables for maximum purity. A general JSA can be decomposed into its Schmidt modes,

$$F(\omega_{\mathrm{s}}, \omega_{\mathrm{i}}) = \sum_j \sqrt{\lambda_j} f_j(\omega_{\mathrm{s}}) g_j(\omega_{\mathrm{i}}), \tag{7}$$

where $f_j(\omega_{\mathrm{s}}) g_j(\omega_{\mathrm{i}})$ are an orthonormal set of completely factorable modes. To quantify the factorability, we use the singular value decomposition (SVD), which is the matrix analogue of the Schmidt decomposition. We define the matrix representation of the JSA as $M = A.\Phi$, where A is the matrix corresponding to the pump amplitude and Φ corresponds to the phase-matching function. The SVD is then a factorization of M into three matrices, which will be called I,S and D; the columns of I represent the part of the Schmidt modes relating to the idler, whereas the rows of S represent the modes of the signal and D is a diagonal matrix linking the two. Elements of the diagonal matrix contain amplitudes $\sqrt{\lambda_j}$ and are in descending order of magnitude.

We obtain D from the SVD and calculate Schmidt magnitudes, λ_j, using the following normalization,

$$\sum_j \lambda_j = 1. \tag{8}$$

A completely pure state will be represented by $\lambda_{j=1} = 1$ and $\lambda_{j \neq 1} = 0$. The Schmidt number K is then defined as

$$K = \frac{1}{\sum_j \lambda_j^2}. \tag{9}$$

For a pure state, K will equal 1. For a completely entangled state, there will be an infinite number of Schmidt magnitudes λ, each approaching zero. The sum of the magnitudes will therefore approach zero with the result that $K \to \infty$. We have previously seen that the JSA is defined as $F(\omega_s, \omega_i) = \alpha(\omega_s + \omega_i)\phi(\omega_s, \omega_i)$, where

$$\alpha(\omega_s + \omega_i) = e^{-[(\delta\omega_s + \delta\omega_s)^2 \sigma^2]/2} \tag{10}$$

and

$$\phi(\omega_s, \omega_i) = \left(e^{ikL/2}\right) \left(\text{sinc}\left(\frac{\Delta k L}{2}\right)\right), \tag{11}$$

where $\delta\omega_l = \omega_l - \omega_{l0}$ and ω_{l0} are central frequencies of the signal ($l = s$) and idler ($l = i$) spectra satisfying energy conservation. Following the same steps described in [10], we develop the phase-matching equation around phase-matched frequencies, using a first-order Taylor series in order to express Δk in terms of the group index,

$$\Delta k = 2k_p - k_s - k_i - 2\gamma P$$

$$= 2 \left.\frac{\partial k_p}{\partial \omega}\right|_{\omega_p} \Delta\omega_p - \left.\frac{\partial k_s}{\partial \omega}\right|_{\omega_s} \Delta\omega_{k_s} - \left.\frac{\partial k_i}{\partial \omega}\right|_{\omega_i} \Delta\omega_{k_i}. \tag{12}$$

With the help of energy conservation, we can substitute $\Delta\omega_p$ and find that

$$\Delta k = \frac{(\mathcal{N}_s - \mathcal{N}_p)}{c} \Delta\omega_{k_s} + \frac{(\mathcal{N}_i - \mathcal{N}_p)}{c} \Delta\omega_{k_i}, \tag{13}$$

where $\mathcal{N}_l$ is the group index of mode l. The JSA, and therefore M, can now be expressed as a function of $\Delta\omega_s$ and $\Delta\omega_i$ only. Using the Sellmeier equation [14], we can then generate the group index for a given fibre geometry and study the factorability of the JSA of a given phase-matching function, pump bandwidth and fibre length.

We first look at the purity of the heralded state as a function of pump bandwidths for three different fibre lengths: 20, 40 and 80 cm. The result of the simulation is shown in figure 10(a). As we can see, each fibre length has an optimum pump bandwidth corresponding to a minimum of the Schmidt number. We then plot in figure 10(b) the minimum Schmidt number accessible and the corresponding optimum pump bandwidth as a function of fibre length. This shows that the longer the fibre, the better purity (the lower Schmidt number) we can obtain. It is also interesting to note that the optimum pump bandwidth decreases when the fibre length increases. One explanation is that when the pump bandwidth is wide, both signal and idler are limited in width by the phase-matching function, whereas when it is narrow, both are limited by energy conservation. At the optimum bandwidth, the signal is mainly limited by the phase matching and the idler mainly by energy conservation, and so their state is more factorable. As the fibre length is increased, the phase-matching sinc function decreases in width (equation (11)), thus the pump bandwidth can also be reduced without reaching a region where it limits the signal bandwidth.

Figure 10 shows that even in the case where the pump bandwidth has been optimized, as for a given fibre length, the Schmidt number still does not reach the optimum value of 1. Looking
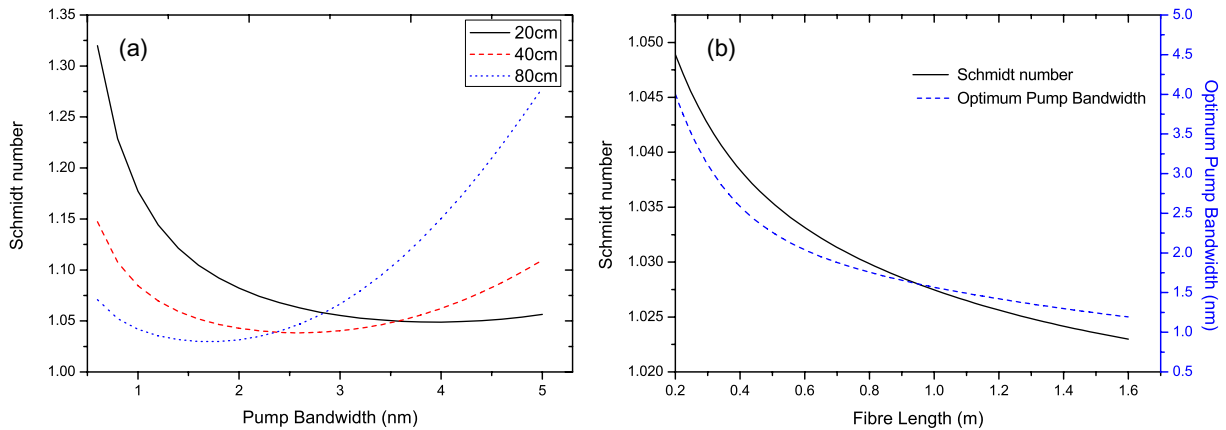
Figure 10. (a) Schmidt number of the heralded state as a function of pump bandwidths for three different fibre lengths: 20, 40 and 80 cm. (b) Minimum Schmidt number and the corresponding pump bandwidth as a function of fibre length.
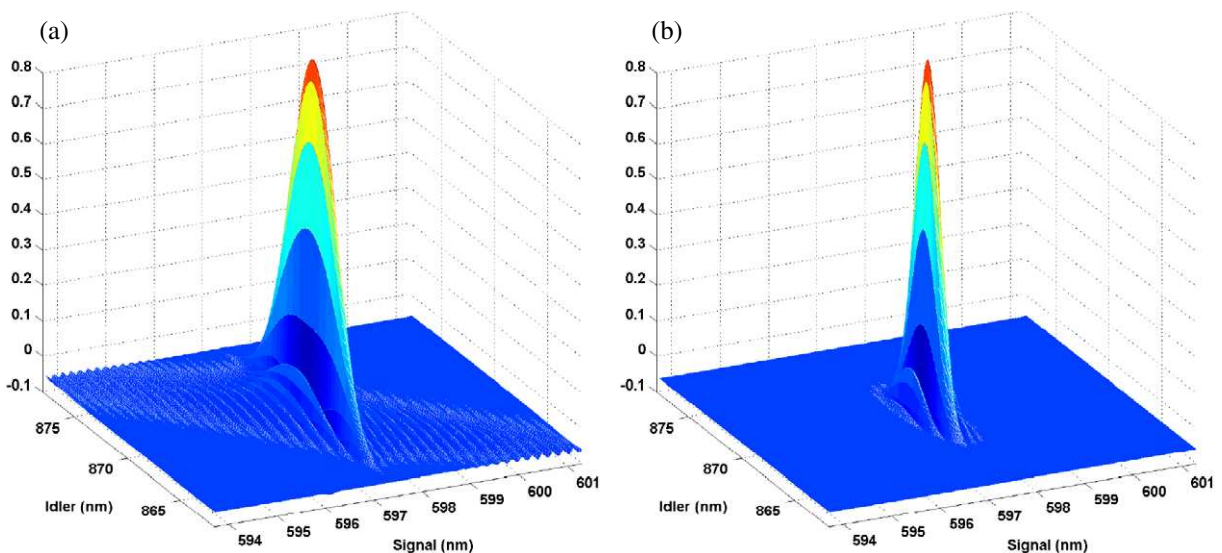

Figure 11. JSA of the created photon pair given by the product of the phase-matching function and the envelope of the pump intensity. (a) Unfiltered case. (b) Where large BFs ($\Delta\lambda_{\text{filter}} \gg \Delta\lambda_{\text{signal/idler}}$) have been applied to both photons.

at the JSA, for example, of a fibre-length of 40 cm (figure 11(a)), we can see that there are still some correlations between signal and idler frequencies coming from the residual ripples of the phase-matching $sinc$ function. These ripples will appear to be small in the measurable spectrum, shown as a Joint Spectral Intensity (JSI) in figure 12 and spectral intensities of the signal and idler in figure 13, but the resulting correlations in the JSA will increase the Schmidt number. One way to enhance the purity of the heralded photon is then to remove these ripples, using BFs whose bandwidths can be much greater than the full-width at half-maximum (FWHM) of the generated photons. This will result in an improvement in the purity without involving significant
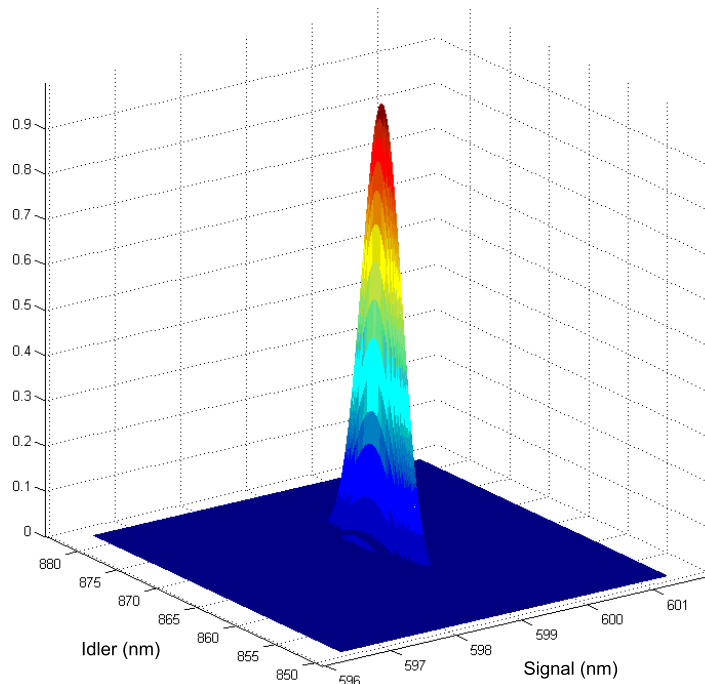
Figure 12. Unfiltered JSI for a length of 40 cm and a pump bandwidth 2.6 nm.
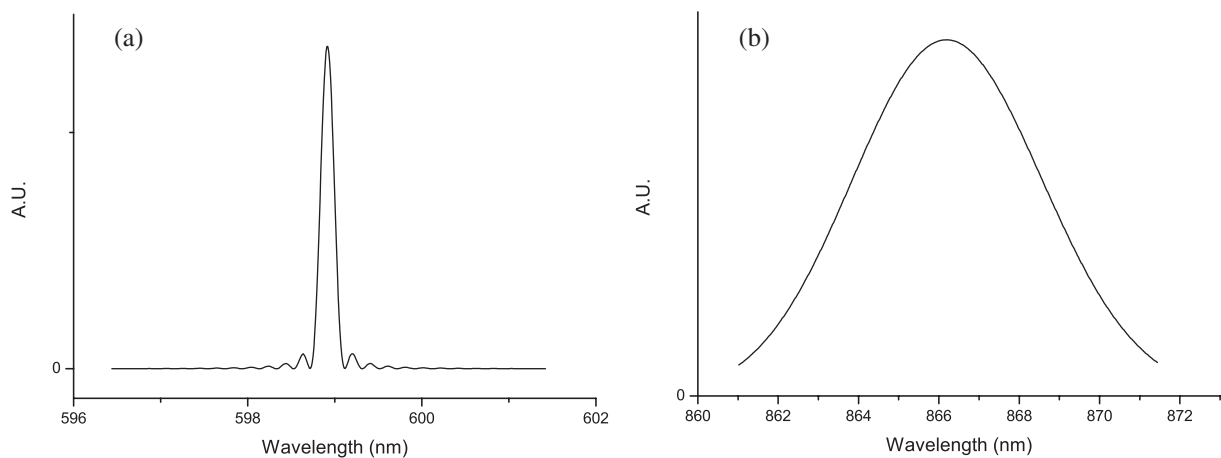
Figure 13. Spectral intensities projected from the JSI for (a) the signal and (b) the idler.

losses in photon collection efficiencies. Figure 11(b) shows the same fibre length as that seen in figure 11(a), where BFs were applied to both signal and idler photon spectra and the pump bandwidth was optimized to this new configuration. As a result, we can see that most of the ripples have disappeared and the calculated Schmidt number has decreased from 1.04 without filters to 1.01 in the filtered case. It is important to note that the photons can still be considered unfiltered since the filters that were used satisfy the following condition: $\Delta\lambda_{\text{filter}} \gg \Delta\lambda_{\text{signal/idler}}$.

We expect the Schmidt number to be related to the HOM dip visibility by $V = 1/K$. To determine whether the HOM dip visibilities seen experimentally were limited by correlations

Figure 14. Comparison of experimental and theoretical Schmidt numbers for a variety of fibre lengths. Black squares show two fibre experiment points while red circles show the bidirectional results.

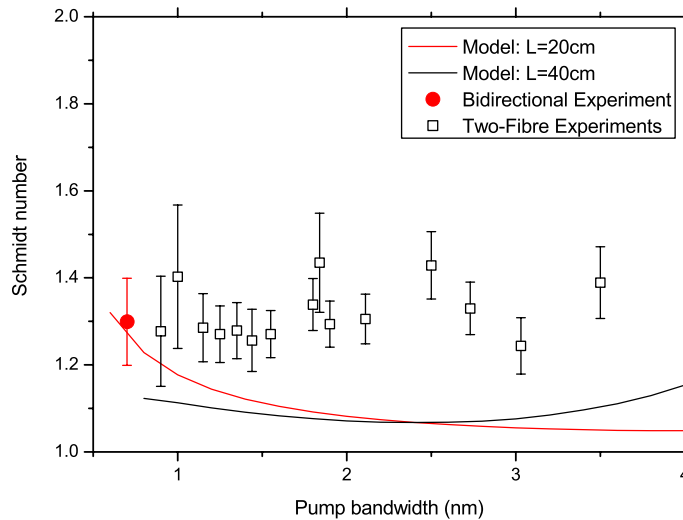in the JSA, we can compare Schmidt numbers derived from experimental results with those obtained from the simulation for a range of pump bandwidths and experimental conditions used. We show in figure 14 that there is an approximately constant offset between the experimental and theoretical results for the two fibres, with the experimental Schmidt numbers never reaching the expected low values of the simulation, suggesting that there is another reason for the lack of photon purity. To test whether this difference arises from the use of two separate pieces of fibre, we can use the visibility of the fringes from the bidirectional case to estimate the Schmidt number of this fibre length and pump bandwidth, and also compare this with the simulation. In doing so, we see in figure 14 that there is no offset present and that the theoretical Schmidt number lies within the error of the experimental point, showing that the lack of visibility could be entirely explained by correlations between signal and idler photons being present in the JSA. This would confirm that the extra loss in visibility in the two-fibre experiments is explained by differences between the two lengths of fibre introducing some cross-source distinguishability.

We can also note that if the bidirectional source was pumped with a larger pump bandwidth of ~4 nm, we can expect a fringe visibility of over 95% and a Schmidt number below 1.05. Further experimental investigation is being carried out to confirm this result. We also note that the pump-filtering method produces top hat pump envelope shapes that increase the Schmidt number from what is achieved through a Gaussian pump envelope of a similar bandwidth.

5. Entangled photon source

The Sagnac loop configuration used above has another intrinsic use when used at lower powers, namely the generation of entanglement. The use of entangled photons is central to many quantum communication and computation schemes [1, 2, 15]; it plays a vital role in the development of quantum repeaters [16] and quantum memories [17]. The Sagnac loop method has been well demonstrated previously for degenerate and non-degenerate photons, both in fibre [18, 19] and using nonlinear crystals [20]; however, all implementations required
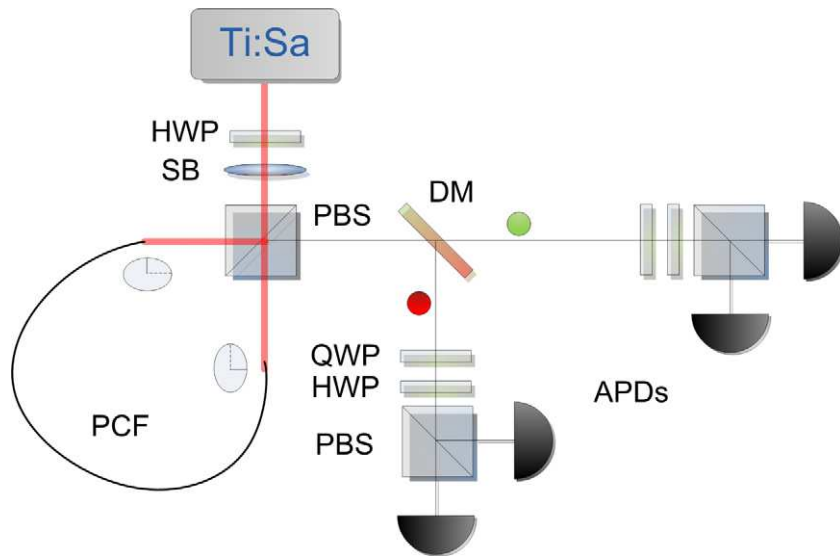
Figure 15. The setup used to generate pairs of entangled photons from a PCF in a Sagnac loop. Pulses from a Ti : sapphire laser are filtered and set to diagonal polarization so that the beam can counter-propagate round a loop of PCF that is twisted, so that the birefringent axis is aligned with the PBS output polarization. Pairs of photons are generated in one of the two directions and then split at a DM. As we have no knowledge of which direction the pairs were generated in, they are in a polarization entangled state. HWP, quarter wave plate (QWP) and PBS combinations allow full state tomography to be carried out.

filtering and therefore suffer from low counting rates. Here we show a demonstration of a source of entangled photons, which are in an intrinsically pure state from a PCF in a Sagnac loop, therefore requiring no narrow spectral filtering.

The setup of this experiment is very similar to that of the bidirectional interference experiment with extra wave plates for analysis and a Soleil–Babinet compensator added, as seen in figure 15. A Ti : sapphire laser emits 100 fs laser pulses ($\sim$8 nm broad) that are then filtered as before, using two diffraction gratings and a slit, down to around 1 nm. This is then passed through a HWP that allows us to set a linear superposition of horizontal and vertical polarizations followed by a Soleil–Babinet compensator consisting of two birefringent crystal wedges that can slide across one another, thereby imparting variable phase ϕ between the horizontal and vertical components. With this combination, any pump state $|\psi\rangle_{\text{in}}$ can be set for the input of the system,

$$|\psi\rangle_{\text{in}} = \alpha|\gamma\rangle_H + \beta \, e^{i\phi}|\gamma\rangle_V. \tag{14}$$

Here we use γ to signify a coherent state of many photons, as are present in the pump pulses. This pulse then enters a PBS that transmits horizontally, and reflects vertically, polarized photons. When two horizontally polarized photons travel in the counter-clockwise direction around the 20 cm loop of PCF, they can generate a vertically polarized signal and idler photons through FWM in the cross-polar regime. These are then converted back to horizontal polarization by a 90° twist in the fibre about the axis of propagation, meaning that $|H\rangle_{P_1}|H\rangle_{P_2} \rightarrow |H\rangle_s|H\rangle_i$. When two vertically polarized pump photons travel in the clockwise

direction, they generate horizontally polarized signal and idler photons that are then twisted back to vertical, and hence we have $|V\rangle_{P_1}|V\rangle_{P_2} \rightarrow |V\rangle_s|V\rangle_i$. The twist in the fibre also ensures that photons propagating in both directions are launched onto the same axis of the PCF, and hence they see the same phase-matching conditions. If we then take into account α and β weightings set by the input HWP, we have the following at detection,

$$|\psi\rangle_{out} = \alpha|H\rangle_s|H\rangle_i + \beta\,e^{2i\phi}|V\rangle_s|V\rangle_i. \tag{15}$$

As the pump is orthogonally polarized to the signal and idler photons, it is automatically rejected back towards the laser, reducing background noise at the output port. We can see from equation (15) that if we set $\alpha = \beta = \frac{1}{\sqrt{2}}$ and $\phi = 0$, then we generate the maximally entangled $|\Phi^+\rangle$ Bell state. It is worth noting that this is an inherently stable setup in that the output state is not affected by temperature fluctuations or vibrations as the relative phase between photons generated in different directions is automatically compensated [21]. The output state does not depend on the length of the fibre or on the point in the fibre where the photons are generated, only on the setting of the input state, making this a very versatile and useful source for quantum information applications. At the output of the PBS, the signal and idler photons are split into two paths by a DM and then collected into optical fibres, each with a PC to compensate for any stress-induced polarization rotations, and are then sent to analysis benches containing a QWP, HWP and PBS. The photons are then launched into multimode fibre and sent to silicon APDs at the transmitted (H) output.

5.1. A test of entanglement

An initial test of entanglement is a measurement of coincidence fringes. The analysis state of one photon of the entangled pair is set on one of two non-orthogonal bases, typically the computational $\{H/V\}$ and diagonal $\{D/A\}$ bases. The other photon is rotated continuously through the basis states and the coincidence rate between detection of both photons is recorded. A second fringe is then measured for the other (non-orthogonal) basis. The classical $\{H/V\}$ basis measurement should yield a coincidence fringe with unit visibility in the absence of all background noise, whereas the $\{D/A\}$ basis measurement should be flat, or have zero visibility, for no entanglement and have unit visibility when the photons are maximally entangled. If the visibility in this basis is greater than 71%, then the state is entangled enough to violate a Bell inequality [22, 23]; this becomes the lower bound, proving that the photons are entangled.

For this test of entanglement, the QWPs can be removed from the analysis benches for the signal and idler photons since we are only concerned with linear polarizations. We choose the idler photon to have the fixed polarization and set the HWP in this arm to be $0°$, or $|H\rangle$, for the $\{H/V\}$ basis and $22.5°$, or $|D\rangle$, for the $\{D/A\}$ basis. For these two positions, we rotate the HWP in the signal analysis bench while recording single APD counts and the coincidence between the signal and idler counts. The result in figure 16 shows a visibility of 98% in the $\{H/V\}$ basis and 90% in the $\{D/A\}$ basis, clearly indicating a high level of entanglement.

The level of entanglement could be reduced by reflections in the fibre [21], excess background noise from residual pump light, Raman photons or most likely from an imbalanced collection of photons from one direction of propagation to the other. This is difficult to correct for because when changing the output of one end of the loop you are changing the input coupling and vice versa, which are often countering each other in quality. This is, however, not a fundamental limit on the amount of entanglement possible with such a setup, which should theoretically produce maximally entangled pairs.
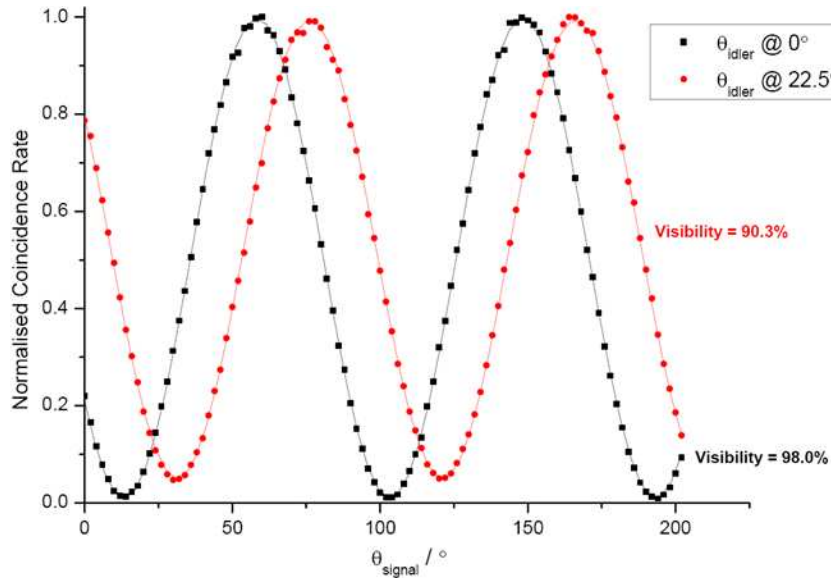
Figure 16. Coincidence count fringes taken with the idler photon fixed at $0°$ in black and $22.5°$ in red, showing 98 and 90% visibility, respectively.

5.2. Quantum state tomography (QST)

A further and more in-depth analysis of the entangled state can be conducted to reconstruct the density matrix of the photon pair, this is known as QST [24]. To perform QST, one must take many copies of the state to be analysed and perform a tomographically complete set of measurements, where the set of measurement operators define a basis in the Hilbert space of the two photon state. In this case, that complete set of measurements is 16 polarization settings as for the HWPs and QWPs in the signal and idler analysis benches. It comprises combinations of analysing $|H\rangle$, $|V\rangle$, $|D\rangle = \frac{1}{\sqrt{2}}(|H\rangle + |V\rangle)$, $|R\rangle = \frac{1}{\sqrt{2}}(|H\rangle - i|V\rangle)$ and $|L\rangle = \frac{1}{\sqrt{2}}(|H\rangle + i|V\rangle)$ states, as shown in table 1.

Using the 16 counts obtained with different measurement settings, we can perform a linear tomographic reconstruction of the state. This does, however, sometimes recreate states that are non-physical since they have negative eigenvalues and since the trace of the square of the density matrix becomes greater than the allowed value of 1. This means that the density matrix $\hat{\rho}$ is not positive semi-definite, as is required. To avoid this problem, we employ a technique, described in [24] and [25], known as the maximum likelihood estimation. This approach estimates the density matrix by first generating a formula of a physical density matrix and then using a likelihood function that quantifies how closely the estimated state would generate coincidences in comparison with the experimental data. This process is then repeated and, using standard numerical optimization techniques, the optimum physical density matrix is found. This process can also be improved by the use of convex optimization techniques [26]. On performing this calculation, we find the closest density matrix to be

$$\hat{\rho}_{\text{exp}} = \begin{pmatrix} 0.446 & -0.033 + 0.021i & 0.002 + 0.055i & 0.382 + 0.042i \\ -0.033 - 0.021i & 0.049 & 0.029 - 0.008i & -0.053 - 0.064i \\ 0.002 - 0.055i & 0.029 + 0.008i & 0.037 & 0.029 - 0.065i \\ 0.382 - 0.042i & -0.053 + 0.064i & 0.029 + 0.065i & 0.467 \end{pmatrix}, \quad (16)$$

Table 1. Wave plate settings for two photon state tomography [24].

ν	State	HWP_s	QWP_s	HWP_i	QWP_i
1	$|HH\rangle$	0	0	0	0
2	$|HV\rangle$	0	0	45	0
3	$|VV\rangle$	45	0	45	0
4	$|VH\rangle$	45	0	0	0
5	$|RH\rangle$	22.5	0	0	0
6	$|RV\rangle$	22.5	0	45	0
7	$|DV\rangle$	−22.5	−45	45	0
8	$|DH\rangle$	−22.5	−45	0	0
9	$|DR\rangle$	−22.5	−45	22.5	0
10	$|DD\rangle$	−22.5	−45	−22.5	−45
11	$|RD\rangle$	22.5	0	−22.5	−45
12	$|HD\rangle$	0	0	−22.5	−45
13	$|VD\rangle$	45	0	−22.5	−45
14	$|VL\rangle$	45	0	22.5	90
15	$|HL\rangle$	0	0	22.5	90
16	$|RL\rangle$	22.5	0	22.5	90

which can be seen graphically in figure 17, split into its real and imaginary parts. Also in figure 17 are the real and imaginary parts of the ideal $|\Phi\rangle^+$ state, which in comparison with our experimentally generated state shows a fidelity of $83.93 \pm 0.08\%$.

We can also quantify the amount of entanglement generated by looking at the Tangle, $\mathcal{T} = 0.5495 \pm 0.0027$, which is greater than 0.5, giving a clear sign that entanglement is generated [24]. The concurrence, $\mathcal{C} = 0.7413 \pm 0.018$, and linear entropy, $\mathcal{L} = 0.3306 \pm 0.0013$, also show a degree of entanglement but are clearly not the optimum values of $\mathcal{C} = 1$ and $\mathcal{L} = 0$. As mentioned before, this non-maximal entanglement is probably due to the $|H\rangle$ and $|V\rangle$ modes not being perfectly overlapped. Nevertheless, this amount of entanglement is already at a useful level and may be improved with careful alignment.

6. Applications and future work

Many additional experiments are possible with this source. The bidirectional source setup, for instance, can be extended to two-photon NOON-state metrology, to show phase measurements with a higher precision than allowed by the standard quantum limit, at very low intensities. Idler photons are used to herald the signal photons, which are injected into a displaced Sagnac interferometer, so that when the phase in one arm of the interferometer is varied, the probability of a coincidence across both outputs shows super-resolution of fringes with a spacing of 312 nm: half the wavelength of the signal and less than half that of the pump. This compares favourably with similar experiments using spontaneous parametric down-conversion sources, where the fringe spacing is equal to that of the pump [27].

By using one entangled source and one single direction correlated source, a teleportation scheme [28] between photons of different wavelengths can be demonstrated. Here, the signal photon from the correlated source heralds the presence of the idler, which can be polarization-encoded to form a qubit using wave plates. When this photon and the idler from the entangled
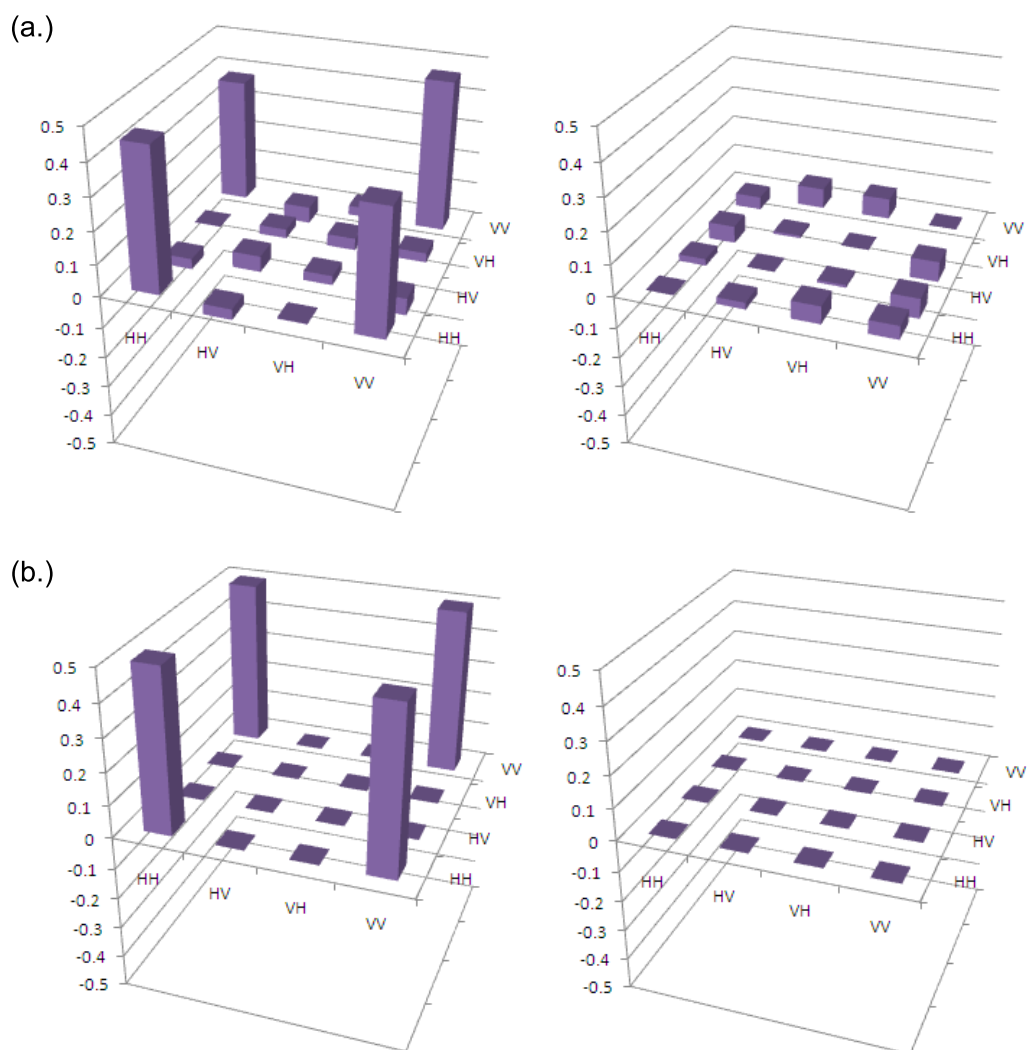
Figure 17. Tomography of the generated entangled state showing (a) the reconstructed real and imaginary parts of the density matrix and (b) the real and imaginary parts of the ideal Φ^+ state. The experimental result shows a fidelity of 84% to the $|\Phi^+\rangle$ state.

source are mixed on a 50 : 50 BS and a coincidence is detected at the two outputs, the two photons have been projected onto a Bell state, and the qubit encoded previously is teleported onto the state of the remaining signal photon from the entangled source following a polarization rotation of 45°. Teleportation has applications in quantum communications, for instance quantum key distribution [1], and in linear optical quantum computing [2], where the success probability of a non-deterministic gate can be improved to an arbitrary level with the addition of teleportation and a resource of entangled ancilla photons.

Similarly, using one entangled source and a correlated source, a scalable version of a quantum CNOT gate can be performed [29], between a control and target qubit encoded in photons of different wavelengths. The successful operation is heralded by ancilla photons, rather than relying on detecting the control and target as in [30–36], which make this CNOT scalable; meaning that it could be used as part of a more complex operation.

IOP Institute of Physics Φ DEUTSCHE PHYSIKALISCHE GESELLSCHAFT

Another application is in the generation of larger entangled states, such as cluster states. In the cluster-state, or one-way, model of quantum computation, a multipartite entangled state is used as a resource for running a quantum algorithm represented by a series of single-qubit measurements [37]. By using two entangled sources and a polarizing BS acting as a fusion gate, we can generate a four photon cluster state and demonstrate quantum gates in the one-way model. Fusion gates are a resource-efficient way of building up cluster states [15], and we can extend this to larger states by adding more entangled pairs and fusion gates or by encoding more qubits in other degrees of freedom, such as path or time-bin encoding.

In conclusion, we have demonstrated a fibre-based source of photon pairs that avoids two significant limitations on the efficiency of conventional down-conversion sources: the flat phase-matching curve means that the photons are created in an intrinsically pure state without the need for spectral filtering, and the photons are created in a single-mode, so we achieve good spatial mode-matching to fibre. We have also shown high visibility non-classical interference between photons from the same and separate sources and generated entangled pairs with a good fidelity to a maximally entangled Bell state. This makes the source suitable for many quantum information applications and future experiments.

Acknowledgments

References

[1] Gisin N and Thew R 2007 Quantum communication *Nat. Photonics* **1** 165–71
[2] Knill E, Laflamme R and Milburn G J 2001 A scheme for efficient quantum computation with linear optics *Nature* **409** 46–52
[3] Nagata T, Okamoto R, O'Brien J L, Sasaki K and Takeuchi S 2007 Beating the standard quantum limit with four-entangled photons *Science* **316** 726–9
[4] U'Ren A B, Silberhorn C, Erdmann R, Banaszek K, Grice W P, Walmsley I A and Raymer M G 2005 Generation of pure-state single-photon wavepackets by conditional preparation based on spontaneous parametric downconversion *Laser Phys.* **15** 146
[5] Soujaeff A, Takeuchi S, Sasaki K, Hasegawa T and Matsui M 2007 Heralded single photon source at 1550 nm from pulsed parametric down conversion *J. Mod. Opt.* **54** 467–71
[6] Garay-Palmett K, McGuinness H J, Cohen O, Lundeen J S, Rangel-Rojo R, U'Ren A B, Raymer M G, McKinstrie C J, Radic S and Walmsley I A 2007 Photon pair-state preparation with tailored spectral properties by spontaneous four-wave mixing in photonic-crystal fiber *Opt. Express* **15** 14870
[7] Grice W P, U'ren A B and Walmsley I A 2001 Eliminating frequency and space-time correlations in multiphoton states *Phys. Rev.* A **64** 063815
[8] Agrawal G P 1995 *Nonlinear Fiber Optics* (New York: Academic)
[9] Hedley T, Knight J, Birks T, Russell P, Pottage J, Bird D and Roberts P 2003 Robust photonic band gaps for hollow core guidance in PCF made from high index glass *Opt. Express* **11** 2854–61
[10] Alibart O, Fulconis J, Wong G K L, Murdoch S G, Wadsworth W J and Rarity J G 2006 Photon pair generation using four-wave mixing in a microstructured fibre: theory versus experiment *New J. Phys.* **8** 67

[11] Hong C K, Ou Z Y and Mandel L 1987 Measurement of subpicosecond time intervals between two photons by interference *Phys. Rev. Lett.* **59** 2044–6

[12] Cohen O, Lundeen J S, Smith B J, Puentes G, Mosley P J and Walmsley I A 2009 Tailored photon-pair generation in optical fibers *Phys. Rev. Lett.* **102** 123603

[13] Mosley P J, Lundeen J S, Smith B J and Walmsley I A 2008 Conditional preparation of single photons using parametric downconversion: a recipe for purity *New J. Phys.* **10** 093011

[14] Hecht E and Zajac A 1974 *Optics* (Reading, MA: Addison-Wesley)

[15] Browne D E and Rudolph T 2005 Resource-efficient linear optical quantum computation *Phys. Rev. Lett.* **95** 010501

[16] Briegel H-J, Dür W, Cirac J I and Zoller P 1998 Quantum repeaters: the role of imperfect local operations in quantum communication *Phys. Rev. Lett.* **81** 5932–5

[17] Hedges M P, Longdell J J, Li Y and Sellars M J 2010 Efficient quantum memory for light *Nature* **465** 1052–6

[18] Xiaoying Li, Voss P L, Sharping J E and Kumar P 2005 Optical-fiber source of polarization-entangled photons in the 1550 nm telecom band *Phys. Rev. Lett.* **94** 053601

[19] Fulconis J, Alibart O, O'Brien J L, Wadsworth W J and Rarity J G 2007 Nonclassical interference and entanglement generation using a photonic crystal fiber pair photon source *Phys. Rev. Lett.* **99** 120501

[20] Fedrizzi A, Herbst T, Poppe A, Jennewein T and Zeilinger A 2007 A wavelength-tunable fiber-coupled source of narrowband entangled photons *Opt. Express* **15** 15377–86

[21] Fulconis J 2006 Fibre source of photon pairs for quantum information *PhD Thesis* University of Bristol, Bristol

[22] Bell J S 1964 On the Einstein–Podolsky–Rosen paradox *Physics* **1** 195–200

[23] Clauser J F, Horne M A, Shimony A and Holt R A 1969 Proposed experiment to test local hidden variable theories *Phys. Rev. Lett.* **23** 880

[24] James D F V, Kwiat P G, Munro W J and White A G 2001 Measurement of qubits *Phys. Rev.* A **64** 052312

[25] Banaszek K, D'Ariano G M, Paris M G A and Sacchi M F 1999 Maximum-likelihood estimation of the density matrix *Phys. Rev.* A **61** 010304

[26] Altazin S 2007 *Masters Thesis* University of Bristol, Bristol

[27] Rarity J G, Tapster P R, Jakeman E, Larchuk T, Campos R A, Teich M C and Saleh B E A 1990 Two-photon interference in a Mach–Zehnder interferometer *Phys. Rev. Lett.* **65** 1348–51

[28] Bouwmeester D, Pan J-W, Mattle K, Eibl M, Weinfurter H and Zeilinger A 1997 Experimental quantum teleportation *Nature* **390** 575–9

[29] Pittman T B, Jacobs B C and Franson J D 2001 Probabilistic quantum logic operations using polarizing beam splitters *Phys. Rev.* A **64** 062311

[30] Clark A S, Fulconis J, Rarity J G, Wadsworth W J and O'Brien J L 2009 All-optical-fiber polarization-based quantum logic gate *Phys. Rev.* A **79** 030303

[31] Pittman T B, Fitch M J, Jacobs B C and Franson J D 2003 Experimental controlled-not logic gate for single photons in the coincidence basis *Phys. Rev.* A **68** 032316

[32] O'Brien J L, Pryde G J, White A G, Ralph T C and Branning D 2003 Demonstration of an all-optical quantum controlled-NOT gate *Nature* **426** 264–7

[33] O'Brien J L, Pryde G J, Gilchrist A, James D F V, Langford N K, Ralph T C and White A G 2004 Quantum process tomography of a controlled-NOT gate *Phys. Rev. Lett.* **93** 080502

[34] Ralph T C, Langford N K, Bell T B and White A G 2001 Linear optical controlled-NOT gate in the coincidence basis. *Phys. Rev.* A **65** 062324

[35] Langford N K, Weinhold T J, Prevedel R, Resch K J, Gilchrist A, O'Brien J L, Pryde G J and White A G 2005 Demonstration of a simple entangling optical gate and its use in bell-state analysis *Phys. Rev. Lett.* **95** 210504

[36] Kiesel N, Schmid C, Weber U, Ursin R and Weinfurter H 2005 Linear optics controlled-phase gate made simple *Phys. Rev. Lett.* **95** 210505

[37] Raussendorf R and Briegel H J 2001 A one-way quantum computer *Phys. Rev. Lett.* **86** 5188–91